

# Pulsed, high-power LED illumination for tomographic particle image velocimetry

Nicolas A. Buchmann · Christian E. Willert · Julio Soria

Received: 9 February 2012/Revised: 14 August 2012/Accepted: 20 August 2012/Published online: 10 October 2012  
© Springer-Verlag 2012

**Abstract** This paper investigates the use of high-power light-emitting diode (LED) illumination for tomographic particle image velocimetry (PIV) as an alternative to traditional laser-based illumination. Modern solid-state LED devices can provide averaged radiant power in excess of 10 W and by operating the LED with short high current pulses theoretical pulse energies up to several tens of mJ can be achieved. In the present work, a custom-built drive circuit is used to drive a Luminus PT-120 high-power LED at pulsed currents of up to 150 A and 1  $\mu$ s duration. Volumetric illumination is achieved by directly projecting the LED into the flow to produce a measurement volume of  $\approx 3$ –4 times the size of the LED die. The feasibility of the volumetric LED illumination is assessed by performing tomographic PIV of homogenous, grid-generated turbulence. Two types of LEDs are investigated, and the results are compared with measurements of the same flow using pulsed Nd:YAG laser illumination and DNS data of homogeneous isotropic turbulence. The quality of the results is similar for both investigated LEDs with no significant difference between the LED and Nd:YAG illumination. Compared with the DNS, some differences are

observed in the power spectra and the probability distributions of the fluctuating velocity and velocity gradients. These differences are attributed to the limited spatial resolution of the experiments and noise introduced during the tomographic reconstruction (i.e. ghost particles). The uncertainty in the velocity measurements associated with the LED illumination is estimated to approximately 0.2–0.3 pixel for both LEDs, which compares favourably with similar tomographic PIV measurements of turbulent flows. In conclusion, the proposed high-power, pulsed LED volume illumination provides accurate and reliable tomographic PIV measurements in water and presents a promising technique for flow diagnostics and velocimetry.

## 1 Introduction

Recent developments in solid-state illumination have led to the rapid availability of high-power light-emitting diodes (LED) whose light output rivals that of conventional light sources. Modern high-power LEDs used in the illumination and automotive industry provide radiometric power in excess of 10 W and are available over a broad range of wavelengths.

For flow diagnostics such as particle image velocimetry (PIV), LEDs offer a number of advantages compared to traditional laser illumination and deserve a closer investigation. For example, Estevadeordal and Goss (2005) use LED illumination for particle shadow velocimetry measurements of micron-sized particles in air and provide some discussions on the pulsed operation of the LED. Similarly, Lindken and Merzkirch (2002) and Broeder and Sommerfeld (2007) use a combination of laser sheet and LED background illumination to study two-phase bubbly flows by means of shadow imaging, PIV and particle

---

N. A. Buchmann (✉) · J. Soria  
Laboratory for Turbulence Research in Aerospace and Combustion, Department of Mechanical and Aerospace Engineering, Monash University, Victoria 3800, Australia  
e-mail: nicolas.buchmann@monash.edu

C. E. Willert  
German Aerospace Center (DLR), Institute of Propulsion Technology, Engine Measurement Systems, Linder Hoehe, 51147 Koeln, Germany

J. Soria  
Department of Aeronautical Engineering,  
King Abdulaziz University, Jeddah, Kingdom of Saudi Arabia

tracking. More recently, Klinner and Willert (2012) use a pulsed inline LED illumination for 3D tomographic shadowgraphy to study liquid droplet formation and breakup in fuel spray injection. Hagsaeter et al. (2008) use a continuous LED illumination in forward scatter for micro-PIV, and Chetelat and Kim (2002) develop a low-cost miniature PIV system with LED illumination in a forward and backward scattering mode. Pulsed LED illumination is also used for schlieren imaging of supersonic turbulent boundary layers (Hargather et al. 2002) and underexpanded, impinging supersonic jets (Buchmann et al. 2011b; Willert et al. 2012).

While in most previous studies, LEDs were used in backlighting or forward scatter mode, PIV commonly requires side-scatter illumination, which demands considerably higher light intensities. Willert et al. (2010) demonstrate that this can be achieved by operating high-power LEDs in pulsed mode and at high currents to produce short light pulses of sufficient energy and duration suitable for planar PIV measurements in water. More recently, LED illumination was already successfully implemented for tomographic PIV applications such as in Kühn et al. (2011) who use an array of 225 LEDs for large-scale illumination of helium-filled soap bubbles and in Buchmann et al. (2010b) where a single high-power LED is used for tomographic PIV measurements of homogeneous turbulence and cylinder wake flow. By briefly overdriving the LEDs with drive currents significantly above their rated threshold level (i.e. 100–200 A), it is possible, depending on the LED, to increase the luminous flux by a factor of 5–8 without damaging the LEDs.

LEDs are mass-produced and are available at very low costs. Compared to traditional laser illumination, LEDs provide an extremely stable pulse-to-pulse light output, both in intensity and spatial intensity distribution. Due to their incoherent light emission and rather wide wavelength range (i.e. 515–535 nm, see Willert et al. (2010) for more details), speckle artefacts and other issues related to laser base illumination are virtually non-existing. The relatively large numerical aperture and uncollimated light emission makes it rather difficult to establish a quality light sheet illumination for planar PIV (Willert et al. 2009), but is less of a restriction for volumetric illumination. Based on this background, the current work investigates the use of volumetric, high-power pulsed LED illumination for tomographic PIV and related 3D particle velocimetry methods, which commonly rely on side-scatter illumination.

The following paper is divided into two parts. The first part describes the pulsed operation of modern high-power LEDs and their performance characteristics when subjected to drive currents of variable magnitude and duration. The second part then investigates the possibility of LED volume illumination by conducting tomographic PIV experiments in homogeneous, grid-generated turbulence. The viability of the proposed LED illumination is assessed by considering turbulent flow statistics and by comparison with similar measurements conducted with pulsed laser illumination as well as DNS data of homogeneous isotropic turbulence.

## 2 Operation of pulsed high-power LEDs

In this paper, two different high-power LEDs of the type PT-120 available from Luminus Device Inc. (Luminus 2009) are investigated and detailed in Table 1. The LEDs are originally designed for projector systems, are available in a range of wavelengths and are amongst the largest colour LEDs currently available. Particularly the red and green PT-120 LEDs are of interest here since modern imaging CCD and CMOS sensors exhibit peak quantum efficiency in the yellow to green range ( $530 \text{ nm} \leq \lambda \leq 550 \text{ nm}$ ). The red LED is selected because of its higher power output compared to the green LED. Contrary to most commonly available LEDs, these devices are surface emitters with a nearly constant light distribution per unit area and are therefore particularly attractive for applications requiring volume illumination due to their large light-emitting area ( $A_{\text{lum}} = 12 \text{ mm}^2$ ). Operating the PT-120 LEDs in continuous mode at the recommended drive current of  $I_{f,CW} = 18 \text{ A}$  produces an averaged radiometric flux of  $\Phi_R = 5.8$  and  $4.7 \text{ W}$  for the red and green LED, respectively. In pulsed operation, the maximum recommended current can be increased to  $I_{f,pulse} = 30 \text{ A}$  at which the red and green LED emit a respective luminous flux of  $\Phi_V = 1,800$  and  $3,500 \text{ lm}$ . This is equivalent to a radiometric flux of  $\Phi_R = 10.4$  and  $7.7 \text{ W}$  at 25 % (red) and 50 % (green) duty cycle. The absolute maximum rated drive current for both LEDs is  $I_{f,max} = 36 \text{ A}$ .

### 2.1 LED drive circuitry

In this study, the high-power LEDs are operated with short-duration high current pulses by an electronic circuitry

**Table 1** Specification of selected high-power LEDs (Luminus 2009)

Emitter	$I_{f,CW}$ (A)	$\lambda_0$ (nm)	$I_{f,pulse}$ (A)	$\Phi_V$ (lm)	$\Phi_R$ (W)	DC (%)	$I_{f,max}$ (A)	$A_{\text{lum}}$ ( $\text{mm}^2$ )
PT-120 (green)	18	525	30	3,500	7.3	50	36	$4.6 \times 2.6$
PT-120 (red)	18	623	30	1,800	10.4	25	36	$4.6 \times 2.6$

shown in Fig. 1. The operation of the circuitry is relative straightforward and resembles that of a switched constant-current driver. Initially, a bank of capacitors are charged through a power supply before releasing the charge to the LED via a TTL-triggered MOSFET power transistor. High pulsed currents and constant operation of the circuitry are achieved by adjusting the resistance between the LED cathode and ground as well as choosing large capacitors with low internal resistance (ESR). A more detailed description of the circuitry including specifications of the individual electrical components is given in Willert et al. (2010). The circuitry is capable of providing pulsed currents of up to  $I_f = 150$  A at pulse durations between  $1 \mu\text{s} \leq \tau_p \leq 250 \mu\text{s}$  at kHz repetition rates.

## 2.2 LED characteristics in pulsed operation

The response of the LED to a current pulse is shown in Fig. 2 for a pulse width of  $\tau_p = 10 \mu\text{s}$  and  $\tau_p = 150 \mu\text{s}$ . The lower trace corresponds to the TTL input pulse, the middle trace to the LED forward current and the upper trace to the emitted light recorded by a fast-response photodiode (Thorlabs, PDA10A). The duration of the LED light emission is directly proportional to the input drive current and can be controlled precisely by the width of the TTL signal. While the rise time of the drive current is almost immediate ( $\tau_{\text{rise}} \approx 500$  ns), the LED lags behind somewhat and reaches a steady light output after approximately  $4 \mu\text{s}$ . After that, the LED light emission closely follows the drive current, which exhibits an exponential decay due to the discharge of the capacitors. At the end of the pulse, a electroluminescence decay time of

approximately  $\leq 2 \mu\text{s}$  exists (Fig. 2b), which results from the recombination of the remaining charge carriers and depends on the LED type and scales with the size of the luminescent area. Compared with other illumination sources (i.e. flashlight, laser, etc.), the delay between the input TTL signal and the start of the light emission is very small ( $\tau_{\text{delay}} \approx 200$  ns) making the LED a very flexible illumination source.

The achievable light emission of the high-power LEDs when driven with short-duration current pulses is illustrated in Fig. 3. Figure 3a shows the increase in mean luminosity versus mean drive current (i.e. the area under the curves in Fig. 2) for the green PT-120 LED and for different pulse durations  $\tau_p = 1, 5, 10$  and  $150 \mu\text{s}$  at  $10$  Hz. The mean light emission is proportional to the drive current for  $\tau_p \geq 5 \mu\text{s}$  irrespective of the drive current. Also plotted in Fig. 3a are data points obtained from the manufacturer (Luminus 2009) for  $\tau_p = 2 \times 10^3 \mu\text{s}$  and  $50\%$  duty cycle, which agree reasonable with the current measurements. In practice, this means that a LED pulsed at  $5 \mu\text{s}$  can be driven up to a maximum current of  $160$  A, which is more than  $5$  times its rated forward current  $I_{f,\text{pulse}}$ . At these operating conditions, the light emission increases by approximately  $3.2$  times compared to the rated specifications. In fact, previous test by Willert et al. (2010) with a similar LED (Luminous, CBT-120) has shown that the forward drive current may even be further increased up to  $I_f = 250$  A without causing noticeable damage to the LED. However, at higher currents, the luminescent efficiency decreases due to saturation effects, which can be seen by comparing the red and green PT-120 LED in Fig. 3b. While at lower currents ( $I_f \leq 80$  A), the red LED exhibits a

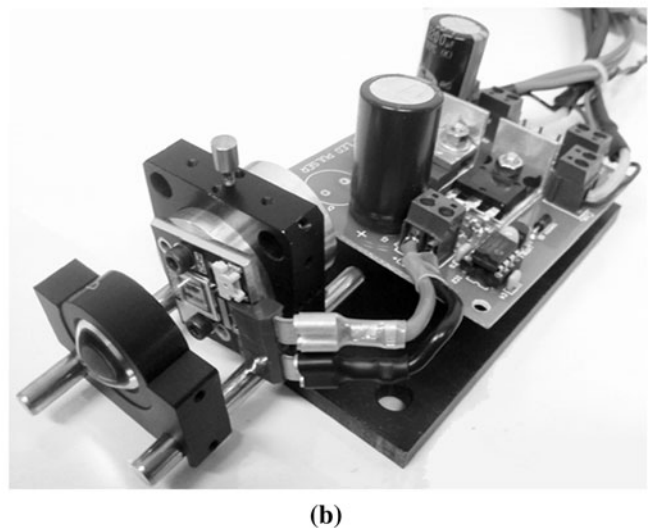
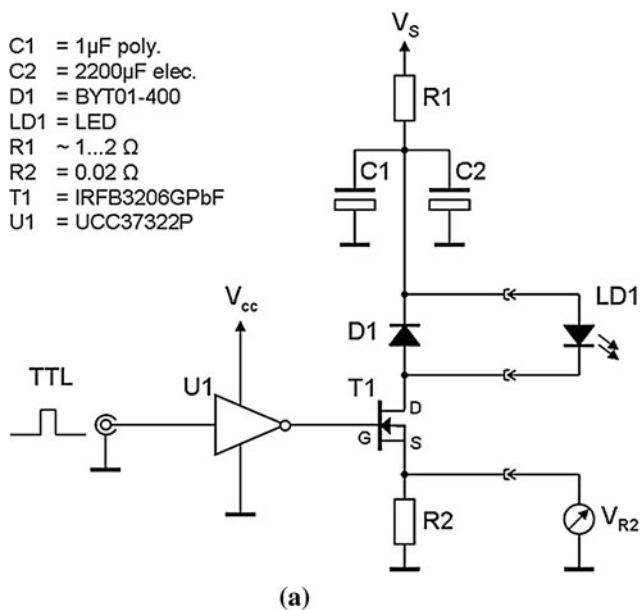


**Fig. 1** Pulsed LED drive circuitry: **a** circuitry diagram; **b** assembled system with PT-120 LED and light focusing optics

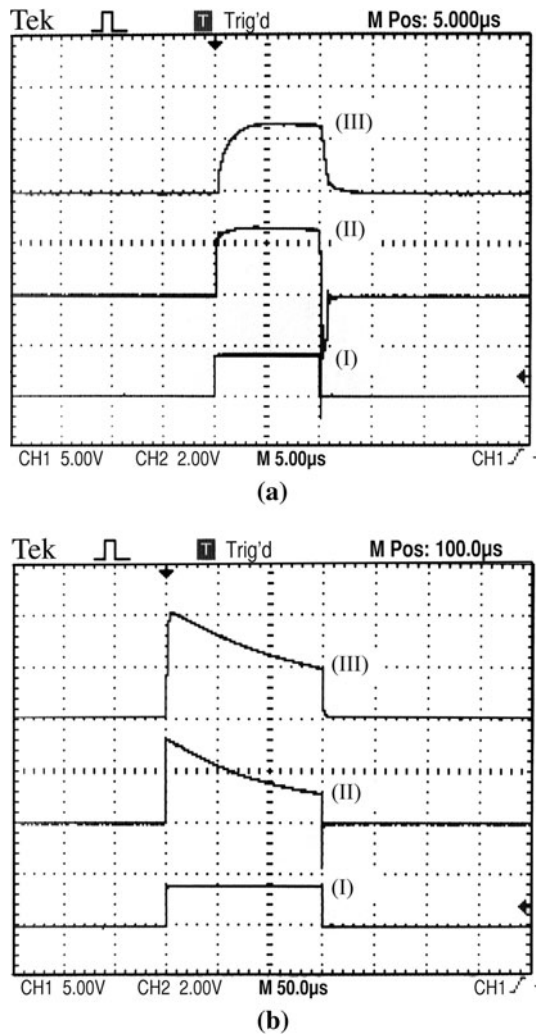


**Fig. 2** LED light emission as detected by a photodiode for a high-power LED (PT-120, *green*) in response to a current pulse and TTL trigger signal: **a**  $\tau_p = 10 \mu\text{s}$ , **b**  $\tau_p = 150 \mu\text{s}$ ; (I) TTL signal, (II) current pulse, (III) photodiode

higher luminescent efficiency (steeper slope), its efficiency decreases above  $I_f > 80 \text{ A}$  compared to the green LED, which exhibits a nearly linear increase in light emission between  $50 \text{ A} \leq I_f \leq 150 \text{ A}$ .

When subjected to high drive currents, the LEDs emit light at shorter wavelength, and it should be noted that the above data are not corrected for the wavelength-dependent response of the photodiode. The photodiode's responsivity decreases towards the blue-green spectral range and therefore the relative luminous flux of the green LED may in fact be higher than reported in Fig. 3. However, most CCD and CMOS also have a decreasing responsivity in this spectral range, which suggest that the above measurements are representative of the relative signal gain at the image sensor.

From the above measurements, the luminous flux (or pulse energy) at a function of drive current can be

approximated. The data sheet for the red PT-120 quotes a radiometric flux of  $\Phi_R = 10.4 \text{ W}$  for  $I_{f,\text{pulse}} = 30 \text{ A}$  and 25 % duty cycle (see Table 1). The effective power over the duration of the current pulse is then 41.6 W. According to Fig. 3b, an increase in drive current to 150 A results in a 3.4 times increase in light emission yielding an effective pulse power of nearly 140 W. This corresponds to a pulse energy of approximately 1.4 mJ assuming a 10  $\mu\text{s}$  pulse. The reason the LEDs can sustain such high drive currents is due to the very short duty cycles  $< 1 \%$ , which allows sufficient cooling of the LED die during pulses.

A more general description of the high-power LED light emission can be obtained by approximating the results in Fig. 3 with the following power law expression:

$$\Phi_{R,\text{est}} = \Phi_R^* \cdot (I_f)^a \quad (1)$$

where  $\Phi_{R,\text{est}}$  is the estimated radiometric flux and  $a$  the power law coefficients obtained via least-squares fit ( $R^2 = 0.994$ ) of expression (1) to the data points in Fig. 3b. The coefficient  $\Phi_R^*$  is the effective pulse power per unit current and is obtained using the radiometric flux quoted in Table 1 at 30 A and adjusted to 100 % duty cycle. The respective coefficients for the red and green LED are  $a_{\text{red}} = 0.76$ ,  $a_{\text{green}} = 0.73$ ,  $\Phi_{R,\text{red}}^* = 3.14 \text{ W/A}$  and  $\Phi_{R,\text{green}}^* = 1.22 \text{ W/A}$ . While both LEDs have nearly the same power law coefficient, the red PT-120 has an approximately 2.5 times higher pulse power, indicating a considerable gain in pulse energy for the red LED.

### 2.3 Damage threshold

The LED damage threshold for a similar high-power LED (Luminous, CBT-120) has previously been established experimentally by Willert et al. (2010) and is again reported in Fig. 4 for completeness. The envelope of 'safe' operation is indicated by the dashed-dotted line and can be divided into three regions that limit the maximum drive current for a given pulse duration. For  $\tau_p \leq 5 \mu\text{s}$  the maximum current is limited to  $I_f \approx 250 \text{ A}$  and decreases log-linear for  $5 \mu\text{s} < \tau_p \leq 150 \mu\text{s}$ , while for  $\tau_p > 150 \mu\text{s}$  the damage threshold approaches the maximum rated forward current of  $I_{f,\text{max}} = 36 \text{ A}$  as given by the manufacturer. For pulse currents above this threshold, the LED will fail rather immediately due to overheating of the bonding wires and the LED die itself.

Knowing the damage threshold of the LED allows an estimation of the maximum achievable pulse energy as a function of  $\tau_p$ . This is also reported in Fig. 4 by calculating the expected pulse energy ( $E_{\text{est}} = \Phi_{R,\text{est}} \cdot \tau_p$ ) for the red PT-120 LED at 85 % of its damage threshold via Eq. (1). As can be seen, the pulse energy increases log-linear for increasing  $\tau_p$  with a slightly lower increase

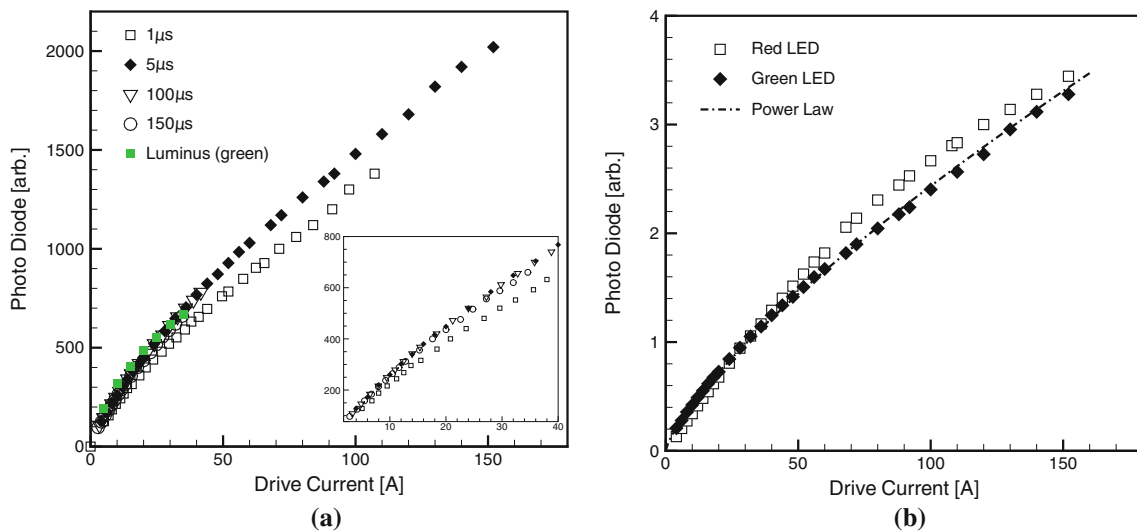


**Fig. 3** Increase in luminosity of a high-power LED: **a** Green LED (PT-120) driven with short-duration current pulses of  $\tau_p = 1, 5, 10$  and  $150 \mu\text{s}$  at  $10 \text{ Hz}$ . *Green symbols* indicate data given by the

manufacturer ( $\tau_p = 2 \times 10^3 \mu\text{s}$ , 50 % duty cycle). **b** Comparison between the red and green PT-120 LED at  $\tau_p = 5 \mu\text{s}$ ,  $10 \text{ Hz}$  and corresponding power law fit

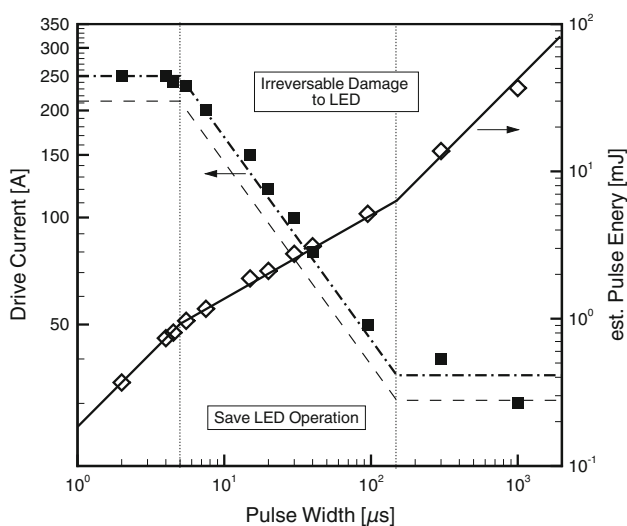


**Fig. 4** Experimentally obtained damage threshold (*filled square*) and maximal achievable pulse energy (*open diamond*). The *dashed line* indicates the drive current at 85 % of the damage threshold used to estimate the pulse energy for the red PT-120

between  $5 \mu\text{s} < \tau_p \leq 150 \mu\text{s}$ . While pulse energies in excess of several tens of mJ are theoretical possible (i.e.  $\tau_p > 10^3 \mu\text{s}$ ), restrictions on the maximum flow velocity typical limit the pulse width to less than a few hundred micro-seconds.

### 3 Tomographic PIV using LED volume illumination

Motivated by the previous measurements, the present investigation uses a single, pulsed high-power LED for

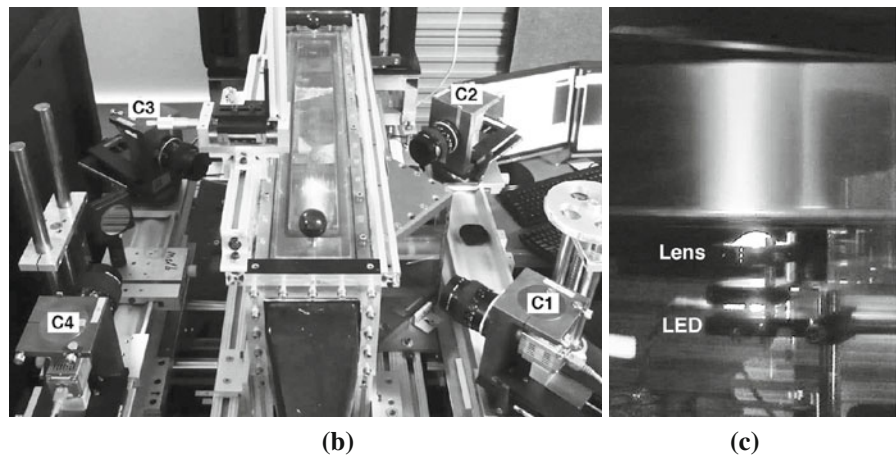
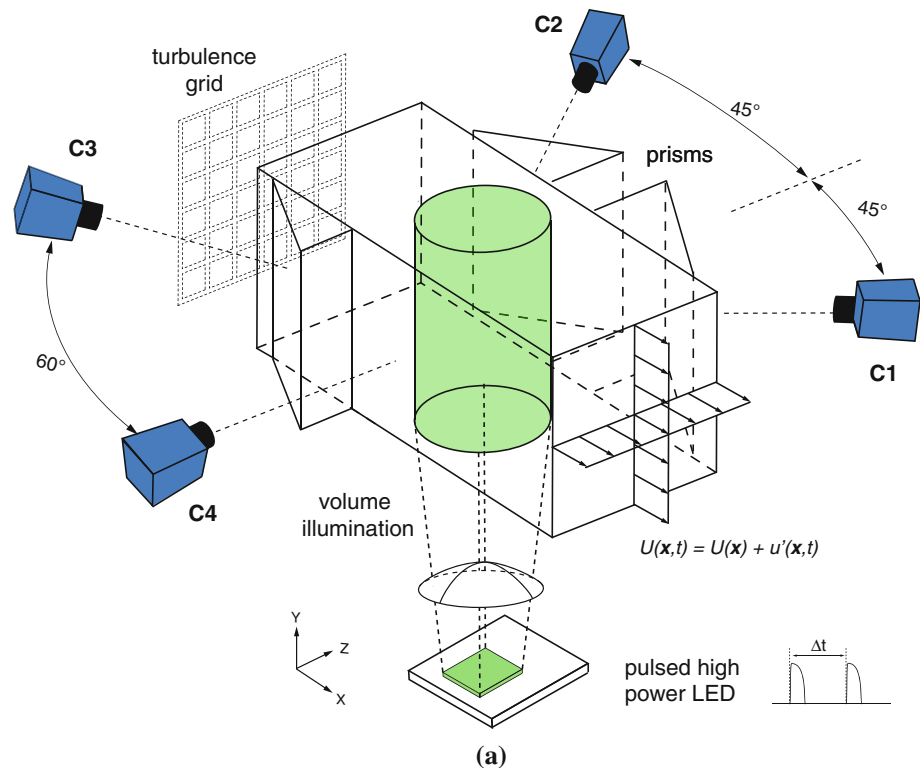
volume illumination of micron-sized particles. This concept is demonstrated in the following by measuring the velocity fluctuations and velocity gradients in a homogeneous, grid-generated turbulent flow by applying homographic PIV.

#### 3.1 Experimental setup

The experiments are conducted in a water channel with cross-section of  $100 \times 100 \text{ mm}^2$  and a length of 1.2 m. The turbulent flow is generated via a rectangular grid located 65 mesh units upstream of the test section. The mesh size is  $M = 8.25 \text{ mm}$  with a solidity of  $\sigma = 0.426$  yielding a mesh size-based Reynolds number ( $\text{Re}_M = U M/\nu$ ) of 900. The tomographic PIV system consists of four digital CCD cameras (PCO PixelFly, 1,240 pixel  $\times$  1,024 pixel), equipped with 55 mm focal length lenses (Micro-Nikkor) and arranged in angles of  $30^\circ, \pm 45^\circ$  and  $90^\circ$  as shown in Fig. 5. The cameras are focused onto an area of approximately  $32.5 \text{ mm} \times 27 \text{ mm}$  with the lens apertures set to  $f^\# = 5.6$  for the first three cameras and  $f^\# = 8$  for the fourth camera. This yields an optical magnification of  $M_{\text{opt}} = 0.18$ , a particle image diameter of approximately  $d_\tau = 2.3$  pixel. Depending on the lens aperture and wavelength of the LED illumination (Table 1), the depth of focus varies between  $\delta_z = 3.5\text{--}8 \text{ mm}$ . The cameras are calibrated using the method proposed by Soloff et al. (1997). A transparent calibration plate containing black dots is traversed through the measurement volume over the interval  $-5 \text{ mm} \leq z \leq 5 \text{ mm}$  in steps of 1 mm with an accuracy of  $\pm 5 \mu\text{m}$ . A volume self-calibration analogous to that of Wieneke (2008) is used



**Fig. 5** **a** Schematic of the experimental setup showing camera and LED arrangement; **b** Photograph showing the water tunnel facility and camera setup; **c** Details of the LED illumination located below the water tunnel. A condenser lens is used to focus the emitted light at the centre of the test section



subsequently to correct the calibration to within 1 pixel accuracy. The relevant experimental parameters are summarised in Table 2.

To provide volume illumination, the luminescent area of the LED is directly projected into the flow field as shown in Fig. 5c. An additional condenser lens is placed in front of the LED to focus the divergent light into the middle of the test section. The flow is seeded with  $36\ \mu\text{m}$  polyamid particles ( $\rho = 1.06\ \text{g/cm}^3$ ) at an equivalent source density of approximately 0.06 particles per pixel (ppp). The LED is operated with  $\tau_p = 150\ \mu\text{s}$  current pulses at  $I_f = 24\ \text{A}$  emitting a single pulse energy of approximately 5.3 and 1.9 mJ for the red and green PT-120 LED, respectively. Consecutive image pairs are recorded at a frame rate of

1Hz with the time separation  $\Delta t$  between two pulses adjusted to 5 ms to obtain a maximum particle image displacement of  $\approx 24\ \text{px}$ .

### 3.2 Volume reconstruction and analysis

Prior to the tomographic reconstruction, the recorded images are pre-processed involving a minimum image subtraction followed by dynamic histogram filtering and Gaussian smoothing with a  $3 \times 3$  kernel. An example of the recorded images before and after processing is given in Fig. 6.

Figure 7 shows the pdf of the recorded raw image intensities for the LED and the Nd:YAG illumination. The

**Table 2** Overview of relevant experimental parameters

Flow	Mesh size	8.25 mm
	Solidity	0.426
	$Re_M$	900
Pulsed, high-power LED	Pulse width	150 $\mu$ s
	max. pulse current	24A
	approx. pulse energy	1.9–5.3 mJ
	Pulse separation	5 ms
Camera	Type	CCD
	Resolution	1,280 $\times$ 1,024 pixel, 12bit
	Pixel size	4.65 $\times$ 4.65 $\mu$ m
	Acquisition rate	1 Hz
Seeding	Type	polyamid spheres
	Diameter	36 $\mu$ m
	Density	1.06 g/cm <sup>3</sup>
Image properties	Lens focal length	55 mm
	Viewing angles	30°, $\pm$ 45° and 90°
	Aperture ( $f^\#$ )	5.6–8
	Diffraction limit	8.3 $\mu$ m
	Image magnification	0.18
	Particle image dia.	2.3 pixel
	Field of view	26 $\times$ 28 $\times$ mm <sup>2</sup>
	max. particle displ.	24 pixel
Seeding density	0.06 ppp	

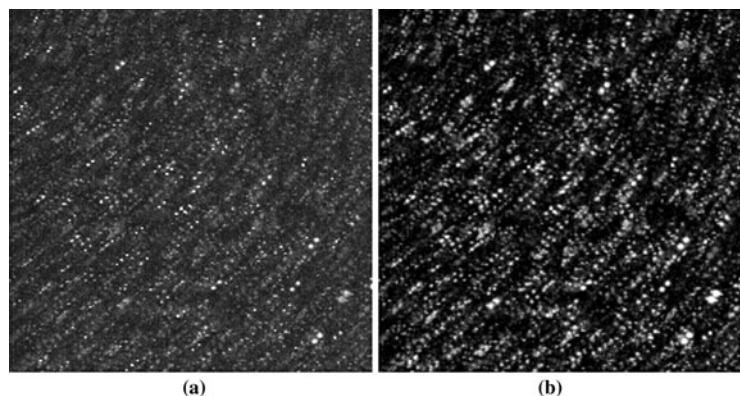
intensity distribution can be divided into a particle image contribution ( $I_p$ ) and a background intensity contribution ( $I_b$ ) (see “Appendix”). The red and green LED illumination produces nearly identical intensity distributions with a mean particle intensity of 226 and 217 counts, respectively. The intensity distribution for the Nd:YAG illumination is broader with a higher mean particle intensity of 491 counts. The dependency of the particle images intensity on the LED forward current is demonstrated in Fig. 8a for the green LED at current pulses of  $\tau_p = 20, 50, 100$  and

150  $\mu$ s. High image intensities are obtained for long light pulses (100–150  $\mu$ s) and large forward currents. The observed increase in particle image intensity can be expressed by a signal-to-noise ratio (SNR) defined as the difference between the particle and background intensity over the noise level of the camera (see “Appendix”). When plotted against the average pulse energy, the curves in Fig. 8a collapse and the SNR follows a power law as shown in Fig. 8b. The power law coefficient of the distribution in Fig. 8b is approximately 0.7 and is close to the coefficient of 0.73 estimated from Fig. 3 for the green LED. The SNR for the red and green LED at the current settings ( $\tau_p = 150 \mu$ s,  $I_f = 24$  A) are approximately 3.6 and 3.2 compared to SNR = 6.9 for the Nd:YAG illumination.

Tomographic volume reconstruction is performed using the multiplicative line-of-sight simultaneous correction reconstruction technique (MLOS-SMART) with an initial solution of unity and 10 iterative corrections of the voxel intensities. A detailed description of this technique is given in Atkinson and Soria (2009), and the interested reader may also refer to the pertinent literature on tomographic volume reconstruction (Atkinson et al. 2011; Elsinga et al. 2006; Kühn et al. 2012; Worth and Nickels 2008) for further details. For the present case, the recorded particle intensities are reconstructed in a volume of size 1,040  $\times$  1,120  $\times$  560 px<sup>3</sup> using a pixel-to-voxel ratio of approximately 1 and a discretisation of 40 voxels/mm. The corresponding physical dimensions of the reconstructed volume are 26  $\times$  28  $\times$  14 mm<sup>3</sup> (or  $x/M \approx 3.2 \times 3.5 \times 1.7$ ).

From the reconstructed particle volumes, the spatial variations of the emitted light intensity are evaluated by plotting the mean intensities (averaged over the volume and 90 realizations) along the  $x$ - and  $z$ - direction in Fig. 9. The volume illumination is approximately circular with the intensity decreasing towards the edges of the measurement volume due to the high divergence of the LED (i.e. large numerical aperture N.A.). At the edge of the light volume, the SNR reduces and out-of-focus effects become

**Fig. 6** Detail of an overlaid PIV recording (256  $\times$  256 px<sup>2</sup>): **a** original image; **b** pre-processed image



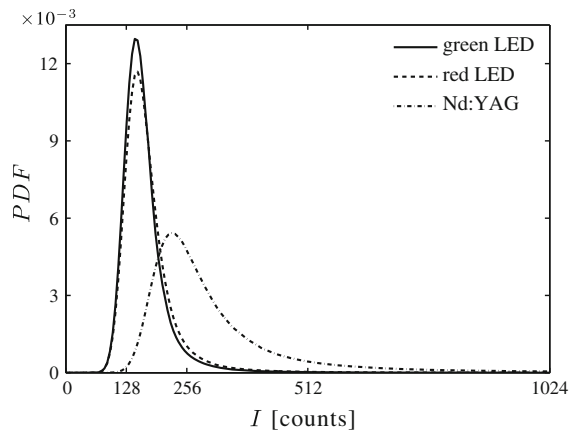


**Fig. 7** Image intensity histogram of the raw images using LED and Nd:YAG illumination. The histograms are normalised to unit area

dominant. The cross-correlation analysis is therefore confined to a domain for which the intensity is larger than 50 % of the peak intensity. This results in an effective measurement volume with approximate cross-section of  $8 \times 8 \text{ mm}^2$ , which is roughly 2–3 times the luminescent area of the LED.

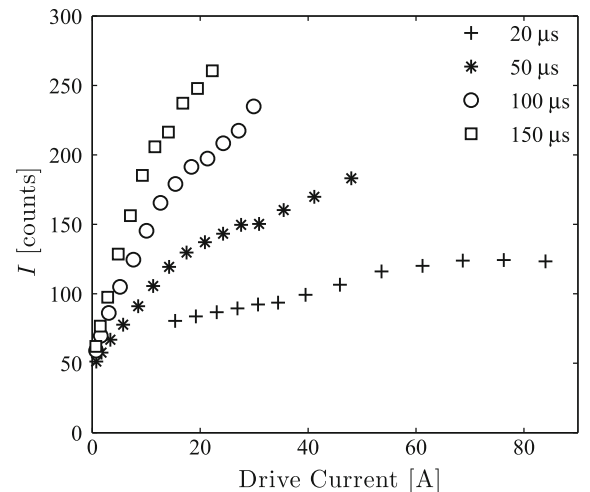
After cropping the reconstructed particle volumes to the above size, the velocity fields are calculated with a multi-grid, multi-pass FFT-based cross-correlation algorithm detailed in Soria (1996) and Atkinson and Soria (2009). Interrogation volumes of  $32^3$  voxels with 75 % overlap are used to provide fields of  $57 \times 117 \times 43$  vectors at a spatial resolution of 0.8 mm and 0.2 mm grid spacing. The calculated vector fields are validated with a normalised median filter and a maximum displacement limit. Invalid vectors are replaced by means of linear interpolation and account for less than 2 % of the total number of vectors.

## 4 Results

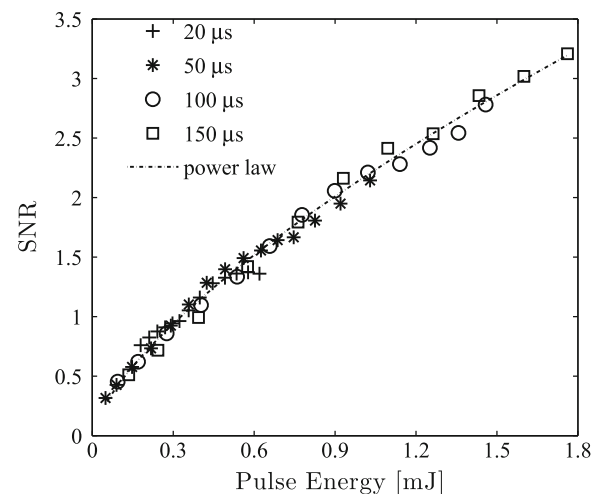
In the following, the performance of the high-power LED illumination is assessed by considering some one-point turbulent statistics and comparison with previous measurements performed with pulsed Nd:YAG laser illumination (Buchmann et al. 2010a) and DNS data of homogeneous isotropic turbulence ( $Re_\lambda = 433$ , Li et al. 2008).

### 4.1 Turbulent flow statistics

The mean flow in the facility exhibits a flat and homogeneous velocity profile in the centre of the test section with a slight increase in the centreline velocity of approximately 4 % over the length of the tunnel due to the growth of the boundary layer and a variation of less than 1 % in the



**(a)**



**(b)**

**Fig. 8 a** Mean particle image intensity versus forward current; **b** Signal-to-noise ratio (SNR) as a function of pulse energy. Data are shown for the green LED (PT-120) operated at 10 Hz with current pulses of  $\tau_p = 20, 50, 100$  and  $150 \mu\text{s}$

cross-stream components. Within the measurement volume, the flow can be assumed nearly constant in the streamwise direction and homogenous in the  $y$ - and  $z$ - directions. The mean velocity profile and turbulent fluctuations in the test section are characterised in detail by Buchmann et al. (2010a); therefore, the following discussion only focuses on the performance of the LED illumination. The turbulent statistics, computed from 90 instantaneous realisations ( $>3 \times 10^6$  independent samples), are reported in Table 3 and are compared with the previous tomographic PIV measurements of Buchmann et al. (2010a) under similar conditions. The integral length scale  $\Lambda$  and Taylor micro-scale  $\lambda_g$  are determined from the longitudinal autocorrelation function, which is averaged in the homogeneous directions  $y$  and  $z$ . The instantaneous



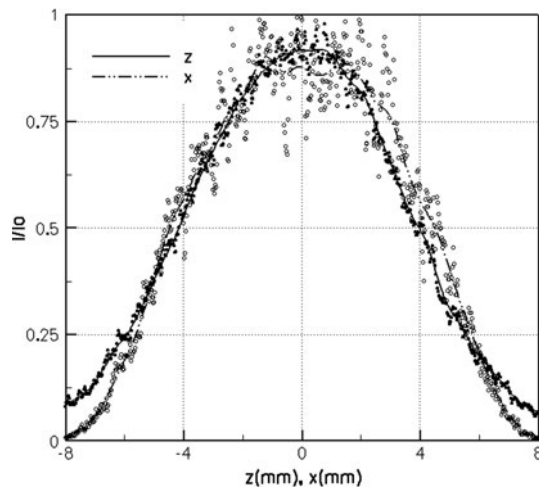


**Fig. 9** Volume averaged particle intensity along the streamwise ( $x$ -) and spanwise ( $z$ -) direction. The extend of the effective volume is estimated at 50 % of the peak intensity

dissipation rate is calculated via  $\varepsilon = 2\nu \times S_{ij}S_{ij}$ , which is used to determine the Kolomogorov length scales. The data reported in Table 3 for the LED and Nd:YAG experiments are in reasonable agreement. The small tunnel dimension and relatively low streamwise velocity produces a non-isotropic flow behaviour ( $u'/v' \approx 0.66 - 0.84$ ,  $u'/w' \approx 0.77 - 0.92$ ) and limits the turbulent Reynolds number ( $Re_\lambda = u'\lambda/v$ ) to approximately  $Re_\lambda \approx 11$ . Between the two experiments, there are some notable differences in the root-mean-square velocity fluctuation  $u'$ , turbulence intensity  $TI$  and dissipation rate. Theses differences are linked to the fact that the LED and Nd:YAG experiments were carried out several months apart, and changes to the facility during this time are likely to have influenced the background turbulence level. In the following, the different experimental and numerical data sets are therefore compared on the basis of their spectral and probability distributions. In this, the DNS data provide a high-resolution, low uncertainty estimate of the turbulent flow characteristics, while the Nd:YAG data are included to provide an example of the more commonly used coherent illumination.

#### 4.2 Velocity field characteristics

Figure 10a shows the longitudinal velocity power spectrum  $E_{11}(k_y)$  for the LED-illuminated flows compared with the Nd:YAG and DNS spectra. At high wavenumbers, the LED spectra become flat and deviate from the true turbulent flow spectrum, represented by DNS, due to a combination of the PIV transfer function effect and experimental noise (see Foucaut et al. (2004) for more details). The smallest resolvable wavenumber is given by the size of the measurement volume, while the largest or cut-off wavenumber

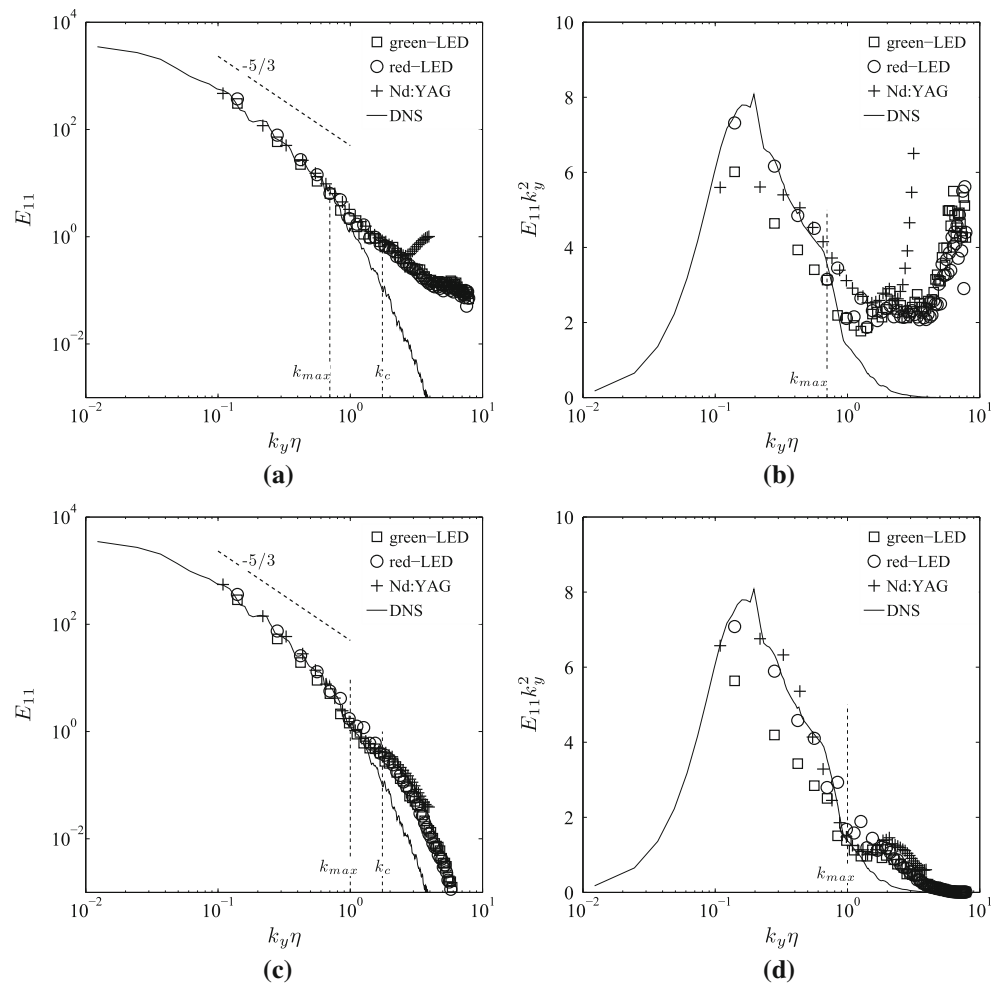
**Table 3** Turbulent statistics for the LED illumination compared to conventional Nd:YAG illumination (Buchmann et al. 2010a)

		LED		Nd:YAG
		Red	Green	
$U$	[mm/s]	121.4	122.3	121.8
$u'$	[mm/s]	3.38	3.25	2.65
$u'/v'$	[-]	0.66	0.71	0.84
$u'/w'$	[-]	0.92	0.94	0.77
$TI$	[%]	2.9	2.7	2.2
$\Lambda$	[mm]	2.48	2.51	2.77
$\varepsilon$	[ $10^{-6} \text{ m}^2/\text{s}^3$ ]	18.53	17.13	7.83
$\eta_k$	[mm]	0.34	0.36	0.43
$\lambda_g$	[mm]	2.72	2.72	3.28
$Re_\lambda$	[-]	11.49	11.05	10.87

is determined by the interrogation window size ( $k_c = 2.8/IW$ ). The effect of noise often means that the effective cut-off ( $k_{max}$ ) is smaller than  $k_c$ , which can be defined as the wavenumber at which the SNR between the measured and true spectrum approaches unity. In the present case,  $k_{max}\eta$  is approximately 0.7 for both LEDs. The pre-multiplied spectra  $k_y^2 E_{11}(k_y)$ , which correspond to the velocity gradient spectra (Ganapathisubramani et al. 2007), are shown in Fig. 10b. At low wavenumbers, the spectra are consistent with the gradient spectrum (or dissipation spectrum) computed from DNS. There is some underestimation of the green LED in this range, but overall the measurements compare favourably for small wavenumbers. At high wavenumbers, the noise influence results in a rapid energy amplification. This means that the mean kinetic energy dissipation estimated from the area under the curve  $k_y^2 E_{11}(k_y)$  includes a large noise contribution at these wavenumbers.

A common procedure to remove high wavenumber noise is a spatial filtering of the measured velocity fields (Worth et al. 2010). Here, a Gaussian shaped convolution filter with a kernel size of  $3\eta \times 3\eta \times 3\eta$  is applied to the fluctuating component of the velocity field. The size of the filter is chosen to match the size of the interrogation window ( $IW \approx 3\eta$ ) and according to Agui and Jimenes (1987) has a spread (i.e. standard deviation) of  $\sqrt{2}\sigma = 1.24\Delta$ , where  $\Delta$  is the vector spacing. The filtered spectra  $E_{11}(k_y)$  and  $k_y^2 E_{11}(k_y)$  are shown in Fig. 10c, d. In comparison with the raw data, Gaussian filtering reduces the effect of noise in the high wavenumber region, resulting in a better agreement between the LED and DNS spectra with  $k_{max}\eta \approx 1$ . The magnitude of the transfer function  $|H(k\eta)|$  of the Gaussian filter kernel is shown in Fig. 12 and is seen to act as a low-pass filter with an exponential decay at high wavenumbers (similar to the true turbulent flow spectrum) and a  $-3\text{dB}$  cut-off at  $k\eta \approx 2.2$ . This filter smoothes the

**Fig. 10** Longitudinal velocity and velocity gradient spectra: **a, b** raw data; **c, d** filtered data



high wavenumbers, which results in a spectrum that more closely follows the DNS and true turbulent flow spectrum. However, filtering cannot ‘improve’ the spectrum, it simply attenuates both noise and true signal indiscriminately over a given wavenumber range determined by the filter. As a result, the energy content of the signal is altered, and the signal can still only be considered accurate up to the cut-off  $k_{\max}\eta \approx 1$  where  $\text{SNR} = 1$  (i.e. ‘peel-off’). Beyond this, the experimental spectra significantly deviate from that of the DNS. A comparison between the LED and Nd:YAG illumination shows that both LEDs exhibit a similar noise level before and after filtering.

An example of the instantaneous fluctuating velocity field is shown in Fig. 11a for a volume of size  $30\eta \times 65\eta \times 24\eta$ . The instantaneous field consists of a range of vortical scales distributed throughout the measurement volume. Figure 11b illustrates contours of normalised vorticity magnitude  $\Omega\eta/U$ , which is determined from the filtered volume data via a second-order central differencing scheme. A region of intense vorticity can be seen at  $y/\eta \approx 10$ .

The probability density function (pdf) of the velocity fluctuations  $u$  normalised by the rms-value is shown in Fig. 13. The experimental data sets are normalised by their respective values reported in Table 3, while the DNS data are normalised by the values given in Li et al. (2008). The distributions for both LEDs are nearly Gaussian, but are slightly positive skewed compared to the Nd:YAG measurement. The respective skewness ( $S$ ) are  $S = 0.18$ ,  $S = 0.29$  and  $S = -0.05$  for the green and red LED and the Nd:YAG data (see Table 4). For the fluctuating velocity components in the respective  $y$ - and  $z$ - directions, a similar behaviour is observed. According to Jimenez (1998), the pdf of the velocity fluctuations is slightly sub-Gaussian (i.e.  $F < 3$ ) as can be seen from the DNS data in Table 4. However, the experimental data exhibit a flatness greater than that of a normal distribution ( $F > 3$ ) due to experimental noise.

The pdf of the longitudinal velocity gradients ( $du/dx$ ) normalised by the Taylor micro-scale,  $\lambda_g$  and the rms of the velocity fluctuations,  $u'$  are shown in Fig. 14a. The ratio  $\lambda_g/u' = (15\nu/\varepsilon)^{1/2}$  characterises the small eddy time-scale

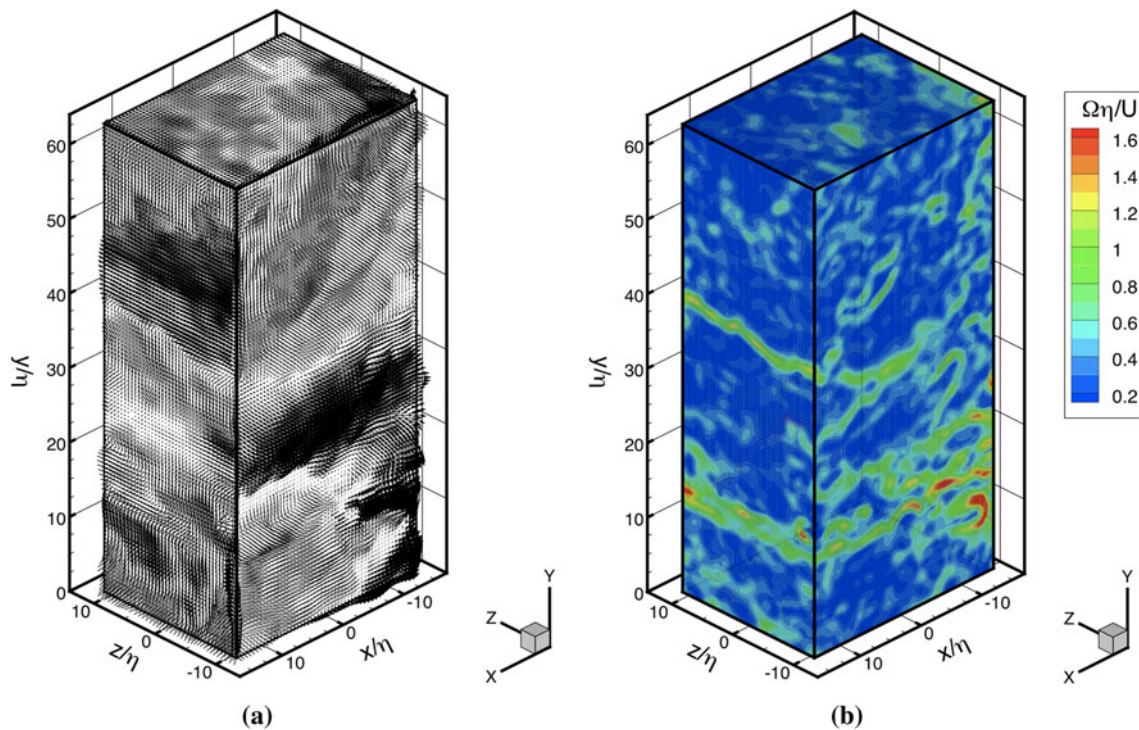


**Fig. 11** **a** Instantaneous fluctuating velocity field; **b** contours of vorticity magnitude normalised by the Kolmogorov length scale

and relates the probability distribution to the smallest resolvable scales (i.e.  $\lambda_g$ ). The distributions for both LEDs are nearly identical, but suffer from spatial resolution effects at very large gradients (i.e. small scale structures). This is consistent with the cut-off in the gradient spectra (Fig. 10d) and can be seen as the ‘peel-off’ from the DNS beyond  $6\lambda_g/u'$ . Nevertheless, for small to medium gradients, the agreement with the DNS data is good. Figure 14b shows the pdfs of the transversal velocity gradients ( $du_i/dx_j$ ), which exhibit a similar trend, but have longer tails than the longitudinal derivatives.

Higher-order moments ( $S$  and  $F$ ) of the above distributions are given in Table 4. The pdf of the longitudinal velocity gradients is non-Gaussian and negatively skewed, which is in good agreement with the DNS. However, the flatness is much higher due to the lack of spatial resolution and increased noise due to ghost particle motion (Elsinga et al. 2011). Similar trends apply to the longitudinal velocity gradients, which are nearly symmetric, but again exhibit a higher flatness than the DNS. Overall, the distributions for the green and red LED are in good agreement with some differences in skewness and flatness, but these are smaller than the deviation from the DNS data.

### 4.3 Measurement accuracy

The measurement uncertainty is estimated by considering the continuity equation (i.e. zero divergence) for incompressible

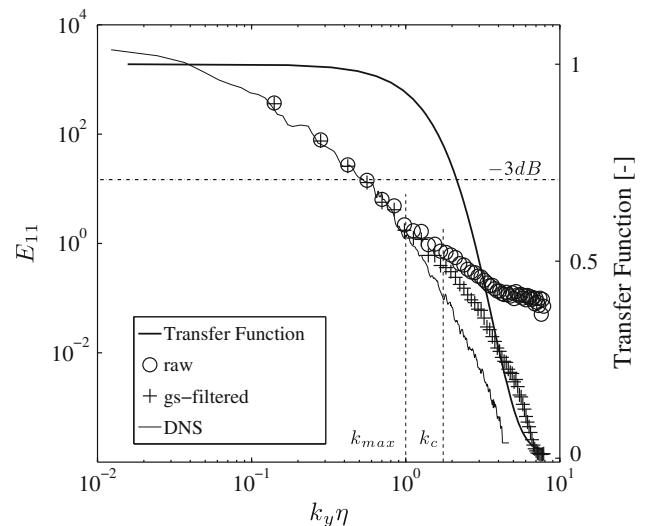


**Fig. 12** Transfer function of the Gaussian filter procedure and corresponding raw and filtered longitudinal velocity spectra (red LED)

flows, where the difference between the calculated divergence  $\nabla \cdot u$  and the zero divergence condition is used to represent the measurement error. Figure 15a shows contours of the joint probability distribution between  $\partial u/\partial x$  and  $-(\partial v/\partial y + \partial w/\partial z)$  normalised by  $\lambda_g/u'$ . Both LEDs exhibit a nearly identical error distribution, which is symmetric and similar to that of the Nd:YAG illumination. The spread of

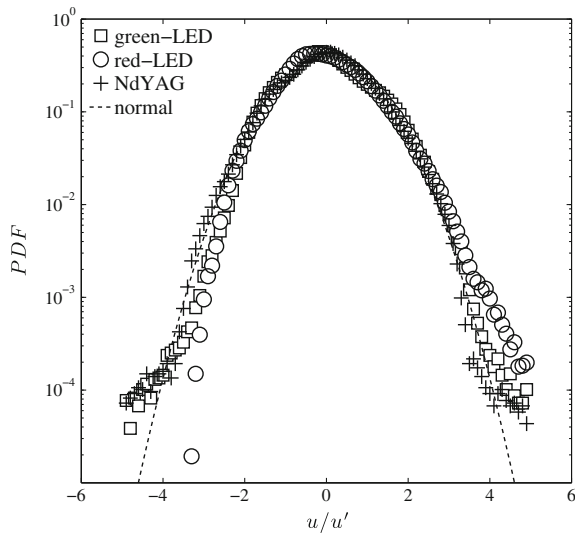


**Fig. 13** pdf of the normalised velocity fluctuation  $u/u'$

**Table 4** Higher-order moments of the streamwise velocity fluctuation  $u$  and its longitudinal and transverse gradients  $\partial u/\partial x$  and  $\partial u/\partial y$

	$u$		$\partial u/\partial x$		$\partial u/\partial y$	
	$S$	$F$	$-S$	$F$	$S$	$F$
Green LED	0.29	5.24	0.22	11.78	0.09	13.35
Red LED	0.18	4.56	0.36	11.25	0.02	8.87
Nd:YAG	-0.05	4.17	—	—	—	—
DNS	0.01	2.72	0.35	4.78	-0.01	6.52
Normal			0	3		

the data around the 45° diagonal (i.e. zero divergence) indicates the divergence error. This error expressed by the rms-value of the distribution is  $1.68 \lambda_g/u'$  for the green LED,  $1.19 \lambda_g/u'$  for the red LED and  $1.26 \lambda_g/u'$  for the Nd:YAG illumination, respectively. Figure 15b plots the dimensional local divergence error distributions  $\nabla \cdot u$  for both LEDs, which closely match that of the Nd:YAG experiment. The respective rms-values of the divergency are 0.011 pixel/pixel, 0.017 pixel/pixel and 0.012 pixel/pixel for the red LED, green LED and Nd:YAG illumination.

When normalised by the norm of the velocity gradient tensor, the rms-values of the local divergence gradient (i.e.  $\nabla \cdot u / \|\nabla u\|$ ) are 0.47, 0.46 and 0.51 for the green LED, red LED and Nd:YAG illumination, respectively. These values compare favourably with a similar study by Worth et al. (2010), who performed tomographic PIV measurement in homogenous isotropic turbulence and reported normalised divergence errors between 0.46 and 0.55. However, it should be pointed out that this normalisation by the velocity gradient tensor norm is inaccurate as it suffers from errors in the velocity gradient tensor itself.

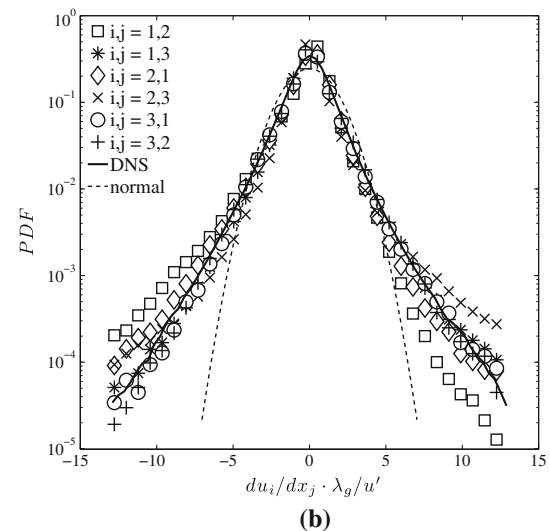
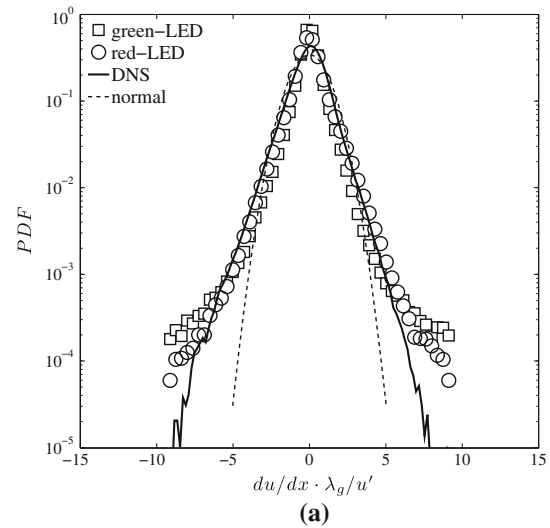


**Fig. 14** One-dimensional pdf for **a** the longitudinal and **b** the transversal velocity gradients

Here, a second-order central difference scheme is used to calculate the velocity gradients. Assuming that both the vector spacing  $\Delta$  and random velocity error  $\sigma(u)$  are uniform in all three directions, it can be shown that the error in the divergence is related to the random velocity error as follows (see Atkinson et al. (2011) for more details):

$$\sigma\left(\frac{\partial u_i}{\partial x_i}\right) = \sqrt{\frac{3}{2\Delta^2}}\sigma(u) \tag{2}$$

where  $\sigma\left(\frac{\partial u_i}{\partial x_i}\right)$  is the rms-value of the divergence (non-normalised) plotted in Fig. 15b. Table 5 lists the random velocity errors estimated from the unfiltered data and for different spatial resolutions. The divergence error depending on the spatial resolution varies between the 0.017 and 0.049 pixel/pixel, which is consistent with errors reported by Scarano et al. (2006) (0.02 pixel/pixel) and Atkinson et al. (2011) (0.05 pixel/pixel). The

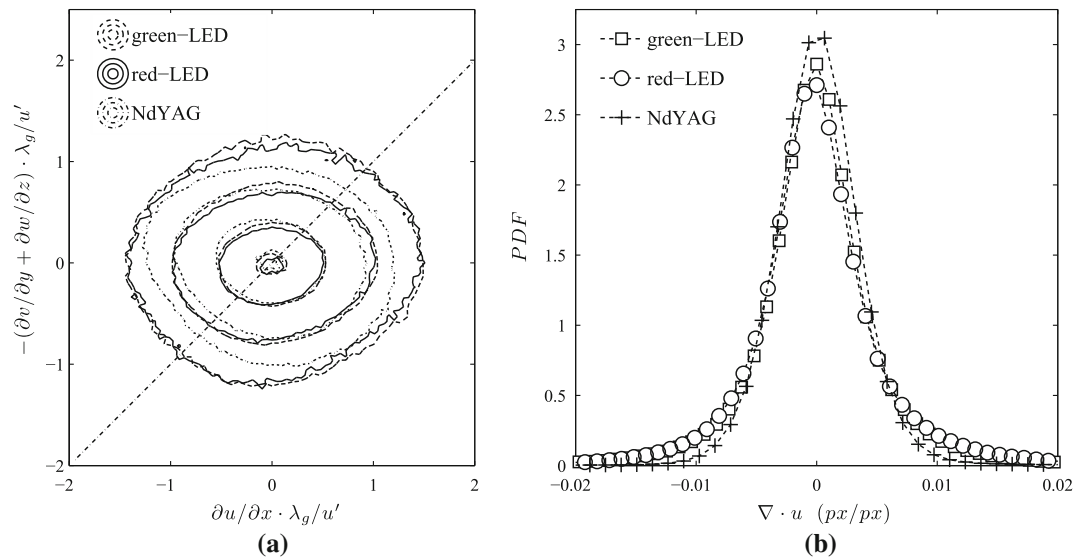


**Fig. 15** Divergence error: **a** joint PDF between  $\partial u/\partial x$  and  $-(\partial v/\partial y + \partial w/\partial z)$  with *contour lines* at [0.05 0.15 0.5 0.95]; **b** PDF of the local divergence error  $\nabla \cdot u$

**Table 5** Divergency error and estimated measurement uncertainty for the unfiltered velocity fields

	$IW$ [px <sup>3</sup> ]	$\Delta$ [px]	$\sigma\left(\frac{\partial u}{\partial x}\right)$ [px/px]	$\sigma(u)$ [px]
Green LED	32	8	0.049	0.32
	32	16	0.023	0.30
	64	32	0.017	0.22
Red LED	32	8	0.031	0.20
	32	16	0.017	0.22
	64	32	0.011	0.15
Nd:YAG	64	32	0.012	0.30

corresponding estimated velocity error is 0.2–0.3 pixel and agrees well with the results of Wieneke and Taylor (2006) (0.2 pixel), Worth et al. (2010) (0.2–0.3 pixel) and Buchmann et al. (2011a) (0.1–0.3 pixel).

## 5 Discussion

### 5.1 Pulsed, high-power LED illumination

The described experiment clearly demonstrated the feasibility of pulsed, high-power LED illumination for tomographic PIV in water. The large numerical aperture of the LED results in a highly uncollimated light source, which is problematic for conventional planar PIV illumination (Willert et al. 2010), but volume illumination can be established relatively simple by projection of the light-emitting surface into the test section or directly onto the image sensor. The large LED aperture makes this approach

rather unique and collimation of the light can be achieved to some extent by including additional lenses. The resulting volume illumination is of good quality with virtually no loss in light intensity due to light shaping optics. This makes the LEDs not only an ideal illumination source for tomographic PIV, but also microscopic PIV (Hagsaeter et al. 2008) and volumetric Shadowgraphy (Klinner and Willert 2012).

The amount of light emitted by the LED is proportional to the drive current and pulse duration, which allows the generation of considerable light pulses with pulse energies in excess of 10 mJ for a single LED. Operating the LEDs at high currents and large pulse durations leads to overheating and potentially irreversible damage of the LED. The current measurements are performed at a 3 % duty cycle with current pulses of 24 A and 150  $\mu$ s duration, resulting in light pulses of approximately 5.3 and 1.9 mJ for the red and green PT-120 LED, respectively. According to Fig. 4, this is within the safe operation of the LED, and in fact, no damage to the LEDs was observed during the experiments. The pulse width must not only be selected to prevent damage to the LED, but also to properly match the flow conditions to avoid streaking of the particle images. Here, a maximum streamwise displacement of 24 pixel is used for which particle streaking corresponds to approximately 0.72 pixel (150  $\mu$ s pulses with 5 ms separation). This is smaller than the particle images diameter ( $d_\tau = 2.3$  pixel), and the resulting elongation of the correlation peak can be neglected. Previous planar high-speed PIV measurements with a similar type LED (Willert et al. 2010) in water used 20  $\mu$ s pulses at 50 A producing light pulses of approximately 400  $\mu$ J. The current volumetric LED illumination is only suitable for measurements in water where larger seeding particles can be used due to a better density



matching. In the present case, relatively large particles with a mean diameter of 36  $\mu\text{m}$  and a particle relaxation time of 72  $\mu\text{s}$  are used. These particles scatter approximately twice as much light as the 28  $\mu\text{m}$  particles used in the comparison Nd:YAG measurements in Buchmann et al. (2010a). This needs to be taken into account when interpreting the results in Figs. 7 and 8 where the image SNR is not only proportional to the illumination energy but also the particle size.

The LED illumination can be assembled at very low costs, and multiple LEDs can be bundled together into larger compact arrays to increase the light output and/or the size of the illuminated volume. Due to the uncollimated nature of the LED light, LEDs are less hazardous, but not necessarily eye-safe. They also require a considerably lower supply power than pulsed Nd:YAG lasers. In comparison with pulsed lasers, no pumping of the medium is required meaning that the LEDs can be fired nearly instantly ( $\tau_{\text{delay}} \leq 200$  ns). Furthermore, the pulse repetition rate can be varied freely and does not depend upon a specific pulsing frequency. The LEDs have a broad spectral intensity distribution preventing the formation of speckle patterns and because only one LED emitter is used, pulse-to-pulse intensity variations are practically non-existing. This results in an almost identical illumination of both exposures with good image contrast, which is particularly desirable for tomographic PIV.

## 5.2 LED illumination for tomographic PIV

The tomographic PIV measurements with LED illumination provide very similar results to those obtained by traditional pulsed Nd:YAG laser illumination. The pdfs of the velocity fluctuations obtained from the LED measurements are slightly skewed, but agree reasonable well in flatness with the DNS data. The pdfs of the velocity gradients are also in good agreement with the DNS for small to medium gradients. The distribution of the longitudinal velocity gradients is negatively skewed while the distribution of the transversal gradients is symmetric. The higher flatness results from the limited spatial resolution, the inability to resolve the very large velocity gradients and the contribution of ghost particle motion. As discussed by Elsinga et al. (2011), ghost particles bias the velocity towards the mean (i.e. zero) and reduce the sensitivity of the measurement to turbulent fluctuations. This results in a tighter clustering around the zero mean, which corresponds to the increase in flatness observed in the measurements. This effect is slightly less pronounced for the red PT-120 LED; however, the flatness is significantly greater compared to the DNS in all measurements. The agreement between the LED and Nd:YAG measurements is good with no noticeable difference in ghost particle correlation for either illumination method.

Measurement noise has a significant effect on the estimated velocity gradients as evidenced in the energy spectra by the ‘peel-off’ at high wavenumbers (Fig. 10a, b). A similar behaviour is also observed by Worth et al. (2010) in their tomographic PIV measurements of homogeneous isotropic turbulence, who used Gaussian filtering to shift the ‘peel-off’ to higher wavenumbers. A similar behaviour can be observed in the current data with a shift of the maximum wavenumber,  $k_{\text{max}}$  and a reduction in spectral energy to higher wavenumbers. This produces a spectrum that more closely follows the DNS spectrum up to higher wavenumbers; however, the signal can still only be considered accurate up to approximately  $k\eta = 1$ . Beyond this, filtering reduces both noise and turbulent fluctuations, indiscriminately. Despite different seeding densities (LED: 0.06ppp; Nd:YAG: 0.02ppp), which affect the reconstruction quality, the LED and Nd:YAG measurements show a similar level of spectral noise before and after filtering and suggest that the LED illumination method enables tomographic PIV measurements in water of similar quality.

The random velocity error, estimated from the fluctuating divergence, is approximately 0.15–0.3 pixel and is consistent with the Nd:YAG measurement and values reported in the literature (Buchmann et al. 2011a; Scarano et al. 2006; Wieneke and Taylor 2006; Worth et al. 2010). In fact, the lowest error of 0.15 pixel is obtained for the red LED with interrogation windows of 64 pixel and 50 % overlap. This is slightly lower than the 0.22 pixel for the green LED and 0.3 pixel for the Nd:YAG measurement at the same resolution.

## 6 Conclusion

High-power light-emitting diode illumination is an attractive and viable alternative to traditional laser-based illumination for flow diagnostics and velocimetry. Particularly for tomographic PIV, where volume illumination is of essence, pulsed LED illumination provides a reliable, scalable and easy to implement alternative. Based on this background, the present paper investigated the use of a single high-power pulsed LED illumination system for tomographic PIV measurements of homogeneous, grid-generated turbulence.

Light pulses of significant intensity (1–10 mJ) were obtained by briefly operating the LED at high drive currents and short pulse durations ( $I_f = 24$  A,  $\tau_p = 150$   $\mu\text{s}$ ). Two LEDs of different wavelength (green,  $\lambda = 525$  nm; red,  $\lambda = 623$  nm) were investigated with both LEDs providing sufficient pulse energy and image quality to perform reliable tomographic PIV measurements in water. The uncertainty in the velocity measurements associated with the LED illumination is proximately 0.15–0.3 pixel.

Overall, tomographic PIV with LED illumination provides similar measurement characteristics to those observed in the Nd:YAG experiments, with the results of the statistical analysis being in good agreement with each other. Some larger differences are observed in the turbulent fluctuations, which are caused by the lack of repeatability of the experiment. With further improvements in LED technology occurring quite rapidly, future increases in light output per unit area are very likely within the next few years, which would make pulsed high-power LED illumination a very viable alternative for flow diagnostics and PIV in particular.

**Acknowledgments** This research was supported under the Australian Research Council's *Discovery Project* funding scheme (DP1096474).

## Appendix

The intensity  $I$  of the recorded particle images shown in Figs. 7 and 16 can be expressed as follows

$$I = I_n + I_f + I_p \quad (3)$$

where  $I_n$  is the noise level of the CCD sensor,  $I_f$  the intensity contribution due to flare, reflections and out-of-focus particles and  $I_p$  the particle image intensity. The noise level  $I_n$  can be determined by recording a black image or from the camera specifications. The background intensity  $I_b = I_n + I_f$  is assumed to follow a normal distribution and is obtained by fitting a Gaussian model to the left-hand side of the intensity pdf. The particle image contribution is then obtained as  $I_p = I - I_b$ .

From Eq. 3, the following signal-to-noise ratios can be defined.

$$\text{SNR}_i = \frac{\langle I_p \rangle}{\langle I_b \rangle}; \quad \text{SNR}_s = \frac{\langle I_p \rangle}{I_n} \quad (4)$$

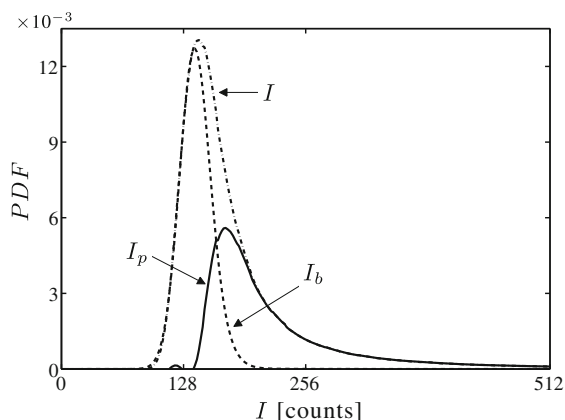


**Fig. 16** Pdf of the image intensity  $I$  (dot dashed line) and its component  $I_p$  (solid line) and  $I_b$  (dashed line)

where  $\langle \rangle$  denotes mean intensities. As the strength of the illumination increases both  $I_f$  and  $I_p$  increase proportionally and  $\text{SNR}_i$  remains nearly constant. The definition of  $\text{SNR}_i$  is equivalent to that of image contrast in Adrian and Westerweel (2010), which is independent of the illumination and promotional to the inverse of the seeding density. For the present case,  $\text{SNR}_i \approx 2$  irrespective of pulse width or drive current. The definition of  $\text{SNR}_s$  is more suitable to characterise the effect of the illumination quality; however, it ignores the contribution of the background intensity. By combining the two definitions, the signal-to-noise ratio expressed as the difference between the particle and background intensity over the noise level is defined as

$$\text{SNR} = \text{SNR}_i \left( 1 - \frac{1}{\text{SNR}_s} \right) \quad (5)$$

Note, in the extreme where the particle image intensity tends to zero (i.e. low light conditions), the SNR also approaches zero.

## References

- Adrian RJ, Westerweel J (2010) Particle image velocimetry. Cambridge University Press, Cambridge
- Agui J, Jimenes J (1987) On the performance of particle tracking. *J Fluid Mech* 185:447–468
- Atkinson C, Coudert S, Foucaut J-M, Stanislas M, Soria J (2011) The accuracy of tomographic particle image velocimetry for measurements of a turbulent boundary layer. *Exp Fluids* 50:1031–1056
- Atkinson C, Soria J (2009) An efficient simultaneous reconstruction technique for tomographic particle image velocimetry. *Exp Fluids* 47:553–568
- Broeder D, Sommerfeld M (2007) Planar shadow image velocimetry for the analysis of the hydrodynamics in bubbly flows. *Meas Sci Technol* 8:2513–2528
- Buchmann NA, Atkinson C, Jermy MC, Soria J (2011a) Tomographic particle image velocimetry investigation of the flow in a modeled human carotid artery bifurcation. *Exp Fluids* 50:1131–1151
- Buchmann NA, Atkinson C, Soria J (2010a) Tomographic and stereoscopic PIV measurements of grid-generated homogeneous turbulence. In: 15th International symposium on applications of laser techniques to fluid mechanics, Lisbon, Portugal
- Buchmann NA, Mitchell D, Ingvorsen KM, Honnery D, Soria J (2011b) High spatial resolution imaging of a supersonic underexpanded jet impinging on a flat plate. In: Sixth Australian conference on laser diagnostics in fluid mechanics and combustion, Canberra, Australia
- Buchmann NA, Willert C, Soria J (2010b) Pulsed, high-power LED volume illumination for tomographic particle image velocimetry. In: 17th Australasian fluid mechanics conference, Auckland, New Zealand
- Chetelat O, Kim KC (2002) Miniature particle image velocimetry system with LED in-line illumination. *Meas Sci Technol* 13:1006–1013
- Elsinga GE, Scarano F, Wieneke B, van Oudheusden BW (2006) Tomographic particle image velocimetry. *Exp Fluids* 41:933–947

- Elsinga GE, Westerweel J, Scarano F, Novara M (2011) On the velocity of ghost particles and the bias errors in Tomographic-PIV. *Exp Fluids* 50:825–838
- Estevadeordal J, Goss L (2005) PIV with LED: Particle shadow velocimetry (PSV). In: 43rd AIAA aerospace sciences meeting and exhibit, pp 12355–12364
- Foucaut JM, Carlier J, Stanislas M (2004) PIV optimization for the study of turbulent flow using spectral analysis. *Meas Sci Technol* 15:1046–1058
- Ganapathisubramani B, Lakshminarasimhan K, Clemens NT (2007) Determination of complete velocity gradient tensor by using cinematographic stereoscopic PIV in a turbulent jet. *Exp Fluids* 42:923–939
- Hagsaeter SM, Westergaard CH, Bruus H, Kutter JP (2008) Investigations on LED illumination for micro-PIV including a novel front-lit configuration. *Exp Fluids* 44:211–219
- Hargather MJ, Lawson MJ, Settle GS, Weinstein LM, Gogineni S (2002) Focusing-Schlieren PIV measurements of a supersonic turbulent boundary layer. In: 47th AIAA aerospace sciences meeting, Florida, Orlando
- Jimenez J (1998) Turbulent velocity fluctuations need not be gaussian. *J Fluid Mech* 376:139–147
- Klinner J, Willert C (2012) Tomographic shadowgraphy for three-dimensional reconstruction of instantaneous spray distributions. *Exp Fluids* doi:10.1007/s00348-012-1308-2
- Kühn M, Ehrenfried K, Bosbach J, Wagner C (2011) Large-scale tomographic particle image velocimetry using helium-filled soap bubbles. *Exp Fluids* 50:929–948
- Kühn M, Ehrenfried K, Bosbach J, Wagner C (2012) Large-scale tomographic PIV in forced and mixed convection using a parallel SMART version. *Exp Fluids* doi:10.1007/s00348-012-1301-9
- Li Y, Perlman E, Wan M, Yang Y, Burns R, Meneveau C, Burns R, Chen S, Szalay A, Eyink G (2008) A public turbulence database cluster and applications to study lagrangian evolution of velocity increments in turbulence. *J. Turbulence* 9(31)
- Lindken R, Merzkirch W (2002) A novel PIV technique for measurements in multiphase flows and its application to two-phase bubbly flows. *Exp Fluids* 33:814–825
- Luminus (2009) Product Data Sheet, PhlatLight PT120 Projection Chipset. Luminus Devices Inc
- Scarano F, Elsinga GE, Bocci E, van Oudheusden BW (2006) Investigation of 3-D coherent structures in the turbulent cylinder wake using tomo-PIV. In: 13th international symposium on applications of laser techniques to fluid mechanics, Lisbon, Portugal
- Soloff SM, Adrian RJ, Liu ZC (1997) Distortion compensation for generalized stereoscopic particle image velocimetry. *Meas Sci Technol* 8:1441–1454
- Soria J (1996) An investigation of the near wake of a circular cylinder using a video-based digital cross-correlation particle image velocimetry technique. *Exp Thermal Fluid Sci* 12:221–233
- Wieneke B (2008) Volume self-calibration for 3D particle image velocimetry. *Exp Fluids* 45:549–556
- Wieneke B, Taylor S (2006) Fat-sheet PIV with computation of full 3D-strain tensor using tomographic reconstruction. In: 13th International symposium on applications of laser techniques to fluid mechanics, Lisbon, Portugal
- Willert C, Moessner S, Klinner J (2009) Pulsed operation of high power light emitting diodes for flow velocimetry. In: 8th international symposium on particle image velocimetry, Melbourne, Australia
- Willert C, Stasicki B, Klinner J, Moessner S (2010) Pulsed operation of high-power light emitting diodes for imaging flow velocimetry. *Meas Sci Technol* 21:075402
- Willert CE, Mitchell DM, Soria J (2012) An assessment of high-power light-emitting diodes for high frame rate schlieren imaging. *Exp Fluids* doi:10.1007/s00348-012-1297-1
- Worth N, Nickels T (2008) Acceleration of Tomo-PIV by estimating the initial volume intensity distribution. *Exp Fluids* 45:847–856
- Worth NA, Nickels TB, Swaminathan N (2010) A tomographic PIV resolution study based on homogeneous isotropic turbulence dns data. *Exp Fluids* 49:637–656